PEDOT: PSS Microchannel based Highly Sensitive Stretchable Strain Sensor

Mitradip Bhattacharjee, Mahesh Soni, Pablo Escobedo, Ravinder Dahiya*

Bendable Electronics and Sensing Technologies (BEST) Group, University of Glasgow, Glasgow, UK, G12 8QQ

*Correspondence to - *Ravinder.Dahiya@glasgow.ac.uk*.

ABSTRACT - This paper presents a flexible microfluidic channel-based strain sensor. The sensor has been developed using a microchannel inside Polydimethylsiloxane (PDMS) substrate. The micro-channel (dia~175 µm) was fabricated using a replica molding technique and filed with conductive poly (3,4-ethylenedioxythiophene) polystyrene sulfonate (PEDOT: PSS) polymer. The developed strain sensor experiences changes in the channel diameter when subjected to various strains, which leads to the changes in the resistance across microchannel having the PEDOT:PSS. The sensor exhibits about 3 order ($\Delta R/R_0$ ~1200) increase in the resistance (R) for 10% applied strain ($\Delta L/L$, L= length of the sensor). This leads to a gauge factor (GF = $(\Delta R/R_0)/(\Delta L/L)$) of ~12000, which is about ~400 times higher than most of the reported polymer-based strain sensors. The sensor was evaluated up to a maximum strain of 30%, which is the standard strain limit associated with human body parts such as fingers and wrists, and it was observed to have a considerably good average degree of hysteresis (< 9%). Further, the sensor was also studied for bending and twisting experiments. A response of ($\Delta R/R_0$ ~250) and ($\Delta R/R_0$ ~300) was recorded for 90° bending and 150° twisting. The sensor showed an electrical resolution of ~150% per degree of free bending and ~12k% per percentage of stretching. Further, demonstrations were performed with robotic and human hand with a control feedback loop. This exhibited the potential application of presented strain sensors in robotics and wearable systems.

KEYWORDS: Strain Sensor, Microchannel, PEDOT:PSS, Gauge Factor, Feedback Control

1. Introduction

Several applications such as wearable electronics[1], human-machine interface[2], robotics and prosthesis[3], and human activity monitoring[4] require measurement of mechanical deformation and strain. Strain sensors are important for the applications that experience bending, for example in prosthesis and robotics applications, where strain sensors could monitor and control the bending of hand joints, fingers, etc.[5]. Similarly, strain sensing is also very important in wearable and flexible electronics, in order to monitor or detect the damaged interconnects due to frequent bending[6]. The advent of flexible and wearable sensor system facilitates the monitoring of different physiological parameters[7] harnessing energy-autonomous solutions[8].

A variety of transduction mechanisms have been implemented for the measurement of strain. The most explored techniques are resistive/piezoresistive[9], strain gauges[10], capacitive[11], optical fiber[12], and piezoelectric[13]. Among these, resistive strain sensors are most frequently used owing to its advantages in fabrication, operation, and calibration processes. In resistive strain sensor the geometrical deformation of the active material with applied strain results in the corresponding change in the electrical resistance. The sensitivity of a strain sensor is defined as gauge factor (GF) which is defined as the ratio of percentage change of sensor response to the applied strain. The metal-foil strain gauges[14] show low values of GF (<5) whereas the semiconductor-based piezoresistive sensors[15] have high values (<200) of GF. A number of previously reported strain and stress sensors are based on nanostructured materials such as Carbon nanotubes (CNT)[16], nanoparticles[17], and nanowires[18]. Most of these devices exhibit piezoresistive properties, thus showing a change in the electrical conductance when the material undergoes a small strain [19]. Apart from these, conductive polymer-based strain sensors have been also reported recently[20]. Among them the conductive poly (3,4-ethylenedioxythiophene) polystyrene sulfonate

(PEDOT:PSS) has gained significant attention owing to its good electrical and structural properties[21]. The PEDOT:PSS based strain sensors are mostly printed between the two electrodes. However, these sensors suffer from environmental effects such as excessive use, temperature, humidity, etc [ref]. Of late, microchannel based strain sensors have been developed using 3D printed techniques[22]. However, the fabrication of a series of uniform microchannels with an economical process is a bottleneck in using these for affordable sensor development. In this direction, our previous work[23] on a stretchable strain sensor based on CNT is relevant as dielectrophoresis (DEP) technique was employed to fabricate the sensors.

In this paper, we present a microchannel based strain sensor. At least 2 order change in resistance was observed across the fabricated sensor for an applied strain up to 30%. The presented sensor is developed using a simple fabrication technique without requiring any external power or dedicated arrangement for deposition of materials/contacts with 10 times superior performance. We present the theoretical basis of strain sensing and comparison with the experimental results, as well as evaluate the effect of bending and twisting on the strain measurements. Furthermore, the application of the presented sensor has been demonstrated in terms of closed-loop control of a 3D printed robotic hand. In our previous study, the percentage strain and maximum change in response were taken into consideration[24], however, here a detailed analysis has been performed, and the fraction strain values and the average change in resistance were considered for the analysis. We observed about 3 order ($\Delta R/R_0$ ~1200) increase in the average resistance (R) value for 10% applied strain ($\Delta L/L$, L= length of sensor). This leads to a gauge factor (GF = $(\Delta R/R_0)/(\Delta L/L)$) of ~12000, which is significantly better (~400 times) than most of the reported polymer[25] and other resistive[26] strain sensors as discussed later in Table S1 in Electronic Supporting Information (ESI). Gauge factor represents the sensitivity of a strain sensor and thus higher GF indicates a

highly sensitive sensor. Apart from this, the proposed sensor showed good linearity up to its maximum starching limit, good resolution in both stretching and bending condition, sufficient dynamic range, and nice stability as discussed later in the paper.

2. Material and Methods

A. Materials: Polydimethylsiloxane (PDMS) was purchased from Sigma Aldrich, and the conductive polymer PEDOT: PSS was procured from Merck, UK. The chemicals were of analytical grade and were used as procured without further purification. The electronic components were purchased from RS Components, UK.
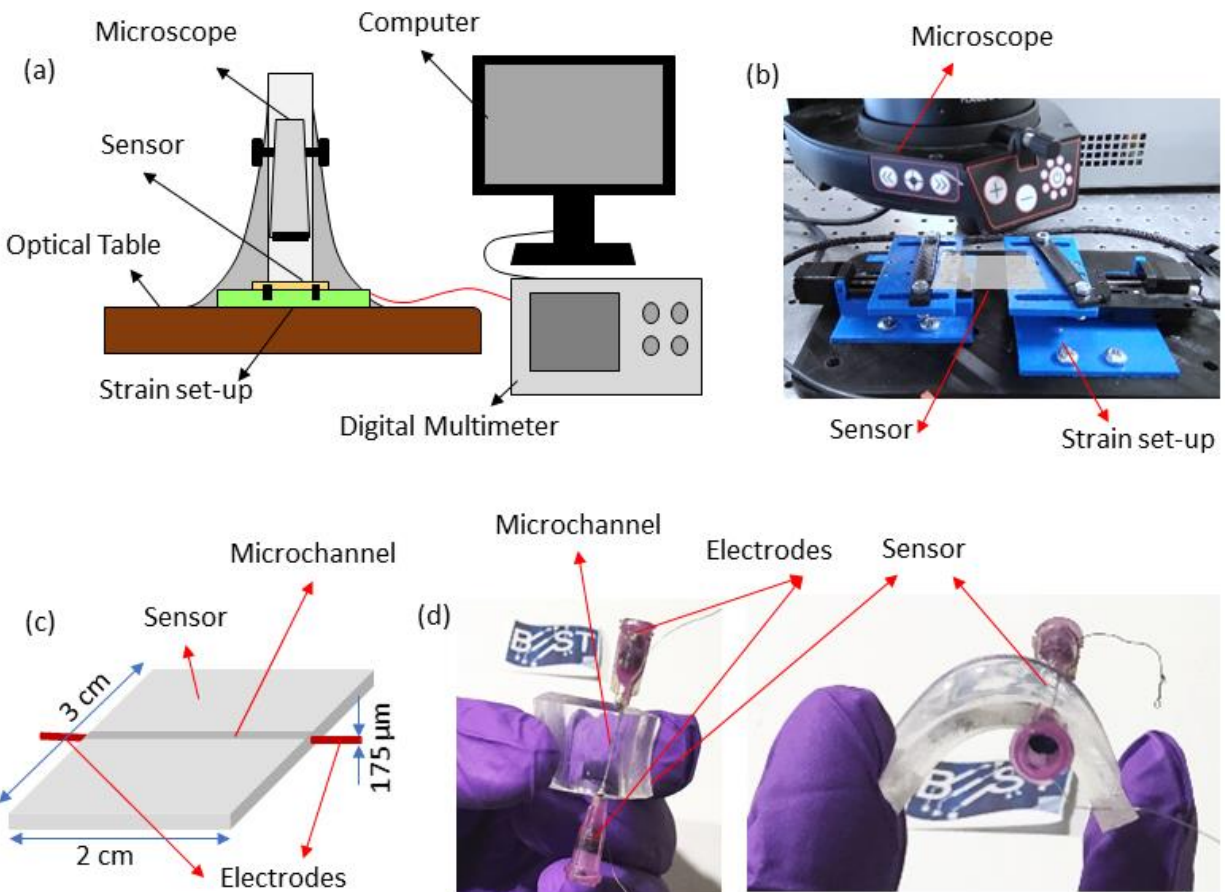
Figure 1: (a) The schematic illustration of the experimental set-up; (b) the real image of the strain set-up employed in the experiments; (c) the schematic illustration of the fabricated strain sensor; (d) the optical image of the flexible sensor.

B. Fabrication: Transparent polymer PDMS was used to fabricate the strain sensor. In this case, the microchannel was fabricated using replica molding technique[27]. In this process, a 10:1 mixture of the PDMS and the cross-linker were prepared and mixed properly using a glass-rod. The prepared mixture was then degassed for 1 hr in vacuum desiccator to ensure that no air bubble was trapped in the mixture. Thereafter, the mixture was poured inside a circular mold of diameter 5.5 cm. A metal wire (dia ~ 275µm) was used in the mold to create the channel inside the PDMS. The mold was then dried in a convection oven for 2 hrs at 70ºC. After drying, the hard PDMS was taken out of the mold and the wire was taken out of the PDMS to form the channel. Thereafter, a syringe was used to inject conducting liquid polymer PEDOT: PSS into the microchannel. The PDMS block was then dried for another 3 hrs at 70ºC. The process of injection and curing was repeated 3 times. The optimization was done by measuring the electrical resistance of the sensor each time after the injection and curing cycle. After this, the fabricated sensor was cut into a rectangular shape of dimension (3 cm × 2 cm) for further experiments. Commercially available cylindrical Al electrodes with dia ~275 µm were then inserted to both ends of the microchannel for electrical connections. A gap of ~1.5 mm was kept inside the microchannel between the two electrodes. The suitable thickness of the sensor was found to be ~3.1 mm. A discussion is added in Section I and **Figure S1(a-b)** of the ESI. The schematic illustration and real images of the experimental set-up and sensor are shown in **Figure 1(a-d)**.

C. Characterization: The strain was applied to the sensor using a LabVIEW controlled strain generation set-up, and the electrical characterization was performed using a digital multimeter

(Agilent 34461A). The strain generation set-up has two holders which are able to move back and forth to generate uniaxial strain with controllable velocity in the sensor, as illustrated in **Figure1 (a-b)**. The sensor was attached to the setup using the holders and thin metallic wires were used to make the electrical connections. A maximum of 30% strain was applied with a velocity of $V_S = $ 0.1, 0.25, and 0.75 mm/s (i.e. strain rates 3.3×10^{-3} %/s, 8.3×10^{-3} %/s, and 25×10^{-3} %/s, respectively). The strain sensor was tested for up to 30% of strain, which is the standard strain limit associated with human skin at different body parts such as fingers, wrists, knee, and elbows for the collagen fibers and tissues to become straitened[28]. The measurement set-up is illustrated in **Figure 1(a,b)**, where image (a) shows the schematic of the experimental set-up and image, and (b) shows the real image of the strain generation set-up. The schematic diagram and real image of the sensor is shown in **Figure 1(c)** and **1(d)**, respectively. The initial experiment was performed for 10% strain with a velocity of 0.1 mm/s as illustrated in **Figure 2(a)**. We observed 3 order ($\Delta R/R_0$ ~1200) changes in electrical resistance. The base resistance, in this case, was ~140 Ω and the resistance at the highest strain was ~180 kΩ. The results are further discussed in detail later in the section. However, the reason behind the change in resistance was the formation of defects and electrical discontinuities in the polymer as discussed in the following section.
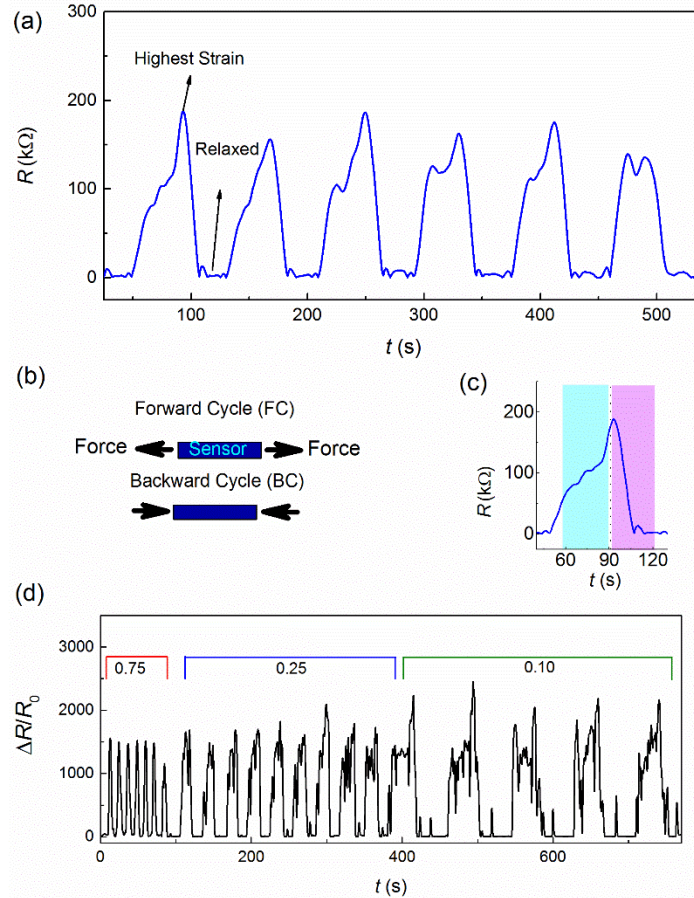
Figure 2: (a) Sensor response under a strain of 10% at 0.1 mm/s velocity; (b) the schematic illustration of forward (FC) and backward cycle (BC); (c) the single cycle of forward and backward movement; (d) response of the sensor at different velocity (0.1, 0.25, 0.75 mm/s) of applied strain.

3. Results and Discussions

A. Strain Sensor Characterisation

The resistance (R_S) value across the sensor was measured as the sensor response. The response of the sensor for a maximum of 10% dynamic applied strain at a speed of $V_S = 0.1$ mm/s is illustrated in **Figure 2(a)**. The resistance across the sensor increased with the strain and then reduced back to its initial resistance with a decrease in the strain value, as illustrated in **Figure 2(a)**. **Figure 2(b)** shows the forward cycle (FC) i.e. increase in the strain and backward cycle (BC) i.e. decrease in the strain schematically. **Figure 2(c)** illustrates one complete cycle consisting of a forward and

backward cycle. It is interesting to see that the recovery of the sensor is faster as compared to the forward cycle. The reason behind this response could be the faster rearrangement of polymer material inside the closed microchannel structure in the backward movement. In this situation, the PEDOT: PSS polymer rearranges back due to the contraction of the sensor to its initial position faster to produce more conductive paths. In case of small deformation, polymer materials hold the memory of the initial positions due to their inherent elastic nature[29]. The sensor was also tested for different speeds of applied strain in the quasi-static and medium-range (generally the case in real-life systems)[30]. **Figure 2(d)** shows the response of the sensor at different speeds (0.1, 0.25, 0.75 mm/s) of applied strain, which corresponds to a strain rate between 0.3 – 2.5 %/s. The sensor showed a stable response for these velocity values.

The strain response of the sensor is shown in **Figure 3**. **Figure 3(a)** shows the image of the sensor at different stretching levels. The sensor showed a significant change in the response as illustrated in **Figure 3(a-b)**. **Figure 3(a)** shows the temporal response of sensor under a strain of 10%, 20%, and 30% at a rate of 0.1 mm/s velocity and **Figure 3(b)** shows both the experimental and theoretical response of the sensor for different strain values. The experimental values are in good agreement with the theoretical one as illustrated in **Figure 3(b)**. The theoretical study is described in the following section to understand the mechanism. The experimental reason of the strain sensing is described in **Section I** of the **ESI**. **Figure S1(c-h)** describes the sensor under relaxed and strained condition with optical and electron microscopic images.
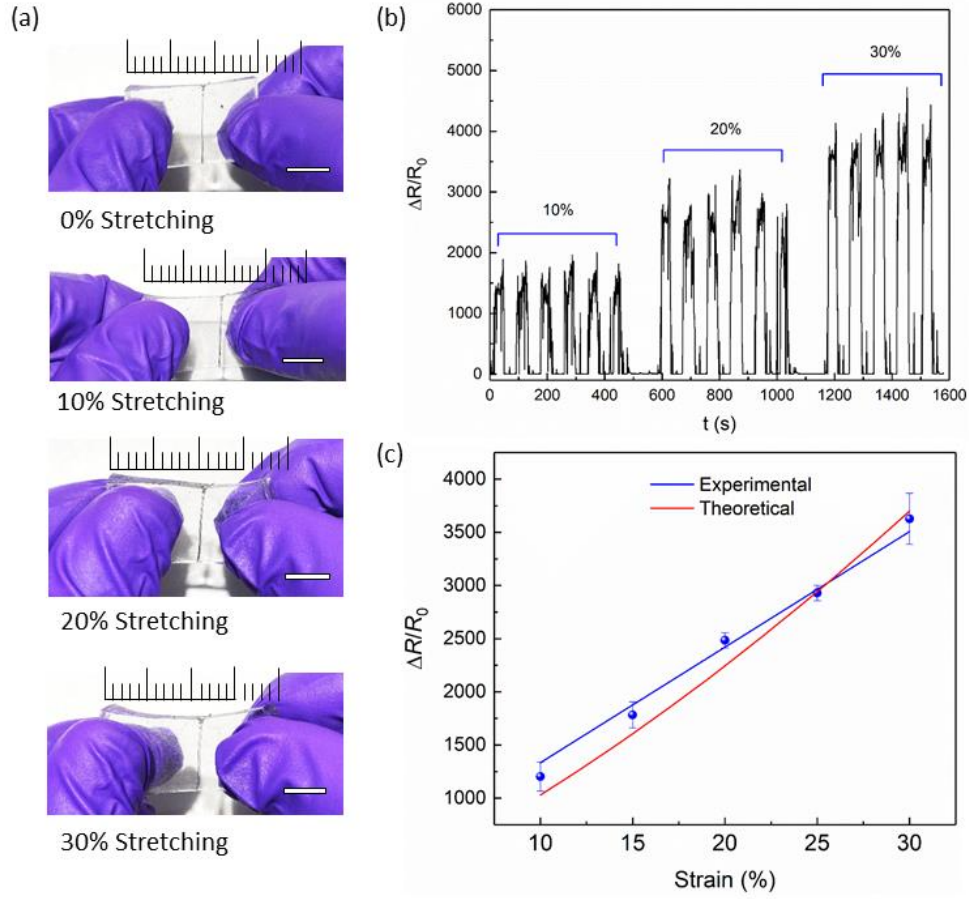
Figure 3: (a) Optical images of the sensor at different stretching levels; (b) Temporal response of sensor under a strain of 10%, 20%, and 30% at a rate of 0.1 mm/s velocity; (c) the response of the sensor (experimental and theoretical) for different strain values.

B. Strain Sensing Mechanism

The electrical conductivity of a composite material depends on the volumetric fraction of the defects and the percolation threshold[31]. Mathematically, this can be defined as $\sigma \propto (V_f - V_c)^s$, where σ is the electrical conductivity, V_f and V_c are the volumetric fraction of the material and the critical volumetric fraction of the filler, respectively. The variable s is the fitting parameter, which is used to best fit the experimental data. In this case, the deformation of the channel reduces the effective volume fraction of the PEDOT:PSS inside the channel due to the formation of electrical

9

discontinuities and defects which lead to the reduction of the conductive path inside the channel. This can be explained by the electrical percolation mechanism. Electrical percolation defines a transition of material from one electrical property to the other (e.g transition from conductor to insulator)[32]. In most of the cases, the composite materials are considered to be the best case for this analysis. However, the geometrical deformation that creates void and electrical discontinuities in a soft material is considered on this occasion. Effectively, in such a scenario the volume fraction of the material changes similar to a composite material.

Considering the PEDOT:PSS is uniformly distributed in the PDMS microchannel, the areal fraction of PEDOT:PSS will be equal to the volumetric fraction of the materials i.e. $V_f = D_f$ and $V_c = D_c$, where D_f and D_c are the corresponding areal fraction values. In this case, the resistance of the sensor increases with the increase in applied strain (**Figure 3(a,b)**) due to the expansion of microchannel (**Figure S1(c-f)**). The volume fraction of the material changes as it creates void spaces due to the formation of electrical discontinuities. The electrical conductivity, in this case, becomes $\sigma \propto \left(D_f - D_c\right)^s$. Since the resistance and conductivity are inversely proportional (i.e. $R = (1/\sigma)(l/A)$, where l is the length of the conductor and A is the cross-sectional area), the relation between R and the D_f and D_c will be $R \propto \left(D_f - D_c\right)^{-s}$.
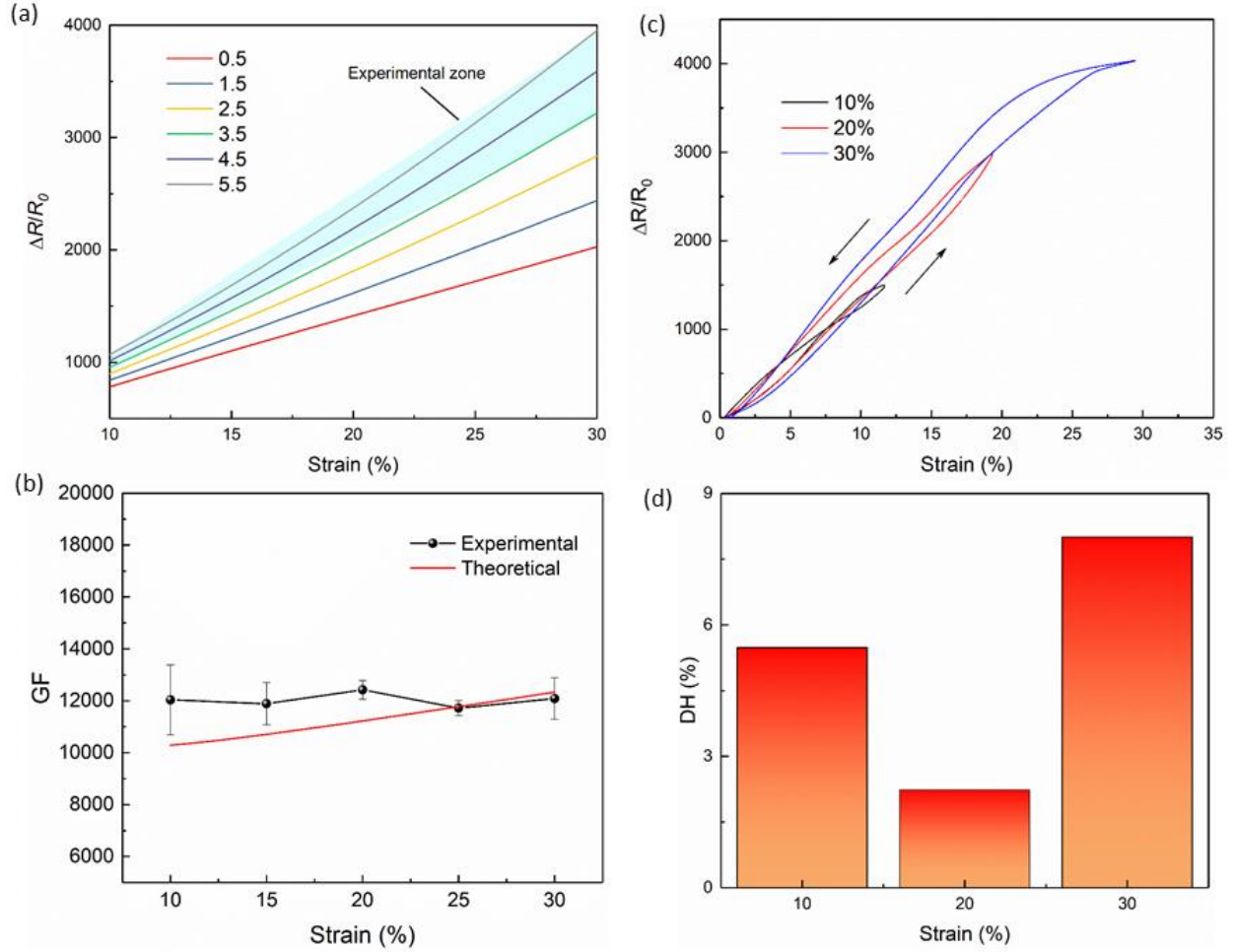
Figure 4: (a) Response of the sensor simulated for different values of m, (b) Gauge factor (GF) (experimental and simulated) of the strain sensor for different strain values, (c) Hysteresis curve of the fabricated strain sensor for different maximum strain values. (d) the average degree of hysteresis (DH) values for different maximum strain values.

In our experiment, the effective length of the channel was 1.5 mm and the diameter of the microchannel is 175 µm (**Figure S1(e)**). The change in the areal fraction D_f depends primarily on two factors: one, the number of electrical discontinuities in the system (N) and second, the magnitude of percentage strain ($\gamma = (\Delta L/L) \times 100$) in the sensor. Further, N is also a function of γ. In low strain region, a linear relation[33] between N and γ is considered, $N = m\gamma + N_0$. The N_0

represents the initial electrical discontinuities present in the system, which is negligible compared to the electrical discontinuities formed after the applied strain and m is the proportionality constant that determines the formation of electrical discontinuities in low strain region. Higher the value of m, higher is the crack formation for the same strain value. Here, m can be defined as $m = (E_1 \times A_1)/(E_2 \times A_2)$ where, E_1 is the young's modulus of active material (i.e. PEDOT:PSS) and A_1 is cross-section of the channel, respectively and E_2 and A_2 are the same parameters for embedded material (i.e. PDMS). In this case, the percolation threshold was determined by considering the formation of electrical discontinuities on the PEDOT:PSS using the formula, $D_c = V_c = (\pi r^2 L)/(8\pi r^2 L + \pi r L^2)$. Where, L and r are the length and radius of the discontinuities, respectively. The typical values of the same were calculated from the FESEM micrograph (**Figure S1(g-h)**) of the same. The theoretical results are in good agreement with the experimental values, as shown in **Figure 3(b)**.

The theoretical study shows that the response of the sensor will be higher if the active material has a higher elastic modulus. This is assuming the same geometrical structure for the embedding material. Thus, a higher *m* value gives a higher response as illustrated in **Figure 4(a)**. The value of m for the materials used ranges between 4.5 to 5.5 indicated as an experimental zone in the plot. Further, the GF was also measured for the proposed sensor and it was also in line with the simulated result as shown in **Figure 4(b)**. The value of GF is considerably high (~12000) compared to other polymer counterparts. **Table S1** in ESI shows the performance comparison between the presented sensor and different flexible strain sensors reported in the literature as stated before. Further, experimental studies were performed for hysteresis study. **Figure 4(c)** shows the hysteresis of the fabricated microchannel based strain sensors for different maximum strain values. The average degree of hysteresis (DH) is calculated[34] using, $DH = (|A_L - A_U|/A_L) \times 100\%$,

where A_L and A_U is the area under loading and unloading curve, respectively. The DH value is obtained for different strain values (10, 20, and 30%) as illustrated in **Figure 4(d)** and it is in the range of $< 9\%$, which is considerably good. Further, the sensor was tested for different bending and twisting conditions and it was found that they are more responsive for higher bending angles as described in Section III of ESI. **Figure S2** illustrates the bending and twisting results of the presented strain sensor. Further, a stability and multiple cycle testing of the sensor was also performed as shown in **Figure S3** of ESI.
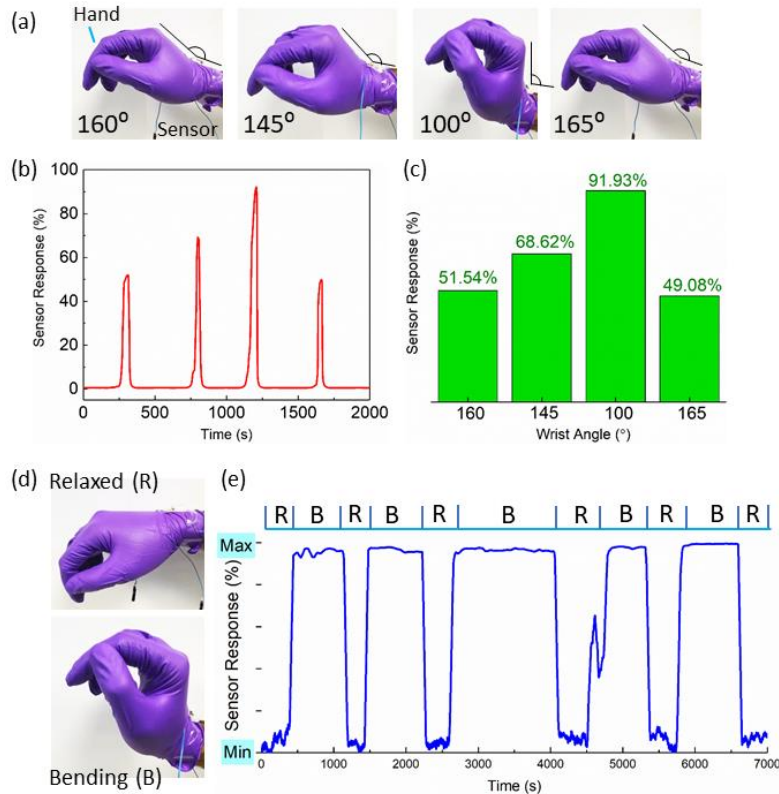

Figure 5: (a) optical image of the hand bent at different angles; (b) the temporal response of the sensor due to the bending; (c) response of the sensor for different bending angles. (d) experimental condition of relaxed (R) and bending (B) condition; (e) temporal response of the sensor for different holding time at maximum bending (B) condition.

C. Application of the Strain Sensor

The sensor was further tested on human and robotic hands after connecting with a system. The sensor response from the system is demonstrated in **Figure 5** and **6**. **Figure 5** shows the response of the sensor for wrist movements when it was fixed with a human wrist using a nitrile glove. The sensor was fixed using a double-sided adhesive tape and then it was connected to a LabVIEW program using a microcontroller-based acquisition circuit (for further details, see Section IV of ESI). The response of the sensor, in this case, was from the designed circuit, which is calibrated as per previously reported results (**Figure 2** and **3**) in this paper. In this case, the response of the maximum stretched condition for this application corresponds to the 100% response of the sensor. **Figure 5(a)** shows the optical image of the experimental condition, placement of the sensor and wrist positions. The corresponding temporal response and the response at different angles are illustrated in **Figure 5(b)** and **5(c)**, respectively. Further, an experiment was also performed at relaxed (R) and bent (B) condition of the wrist as shown in **Figure 5(d)** at different holding time i.e. holding the wrist at the bent condition for different time periods to check the holding response of the sensor. **Figure 5(e)** shows the response of the sensor was quite stable in this condition. A demonstration was performed as shown in Supporting Video S1.
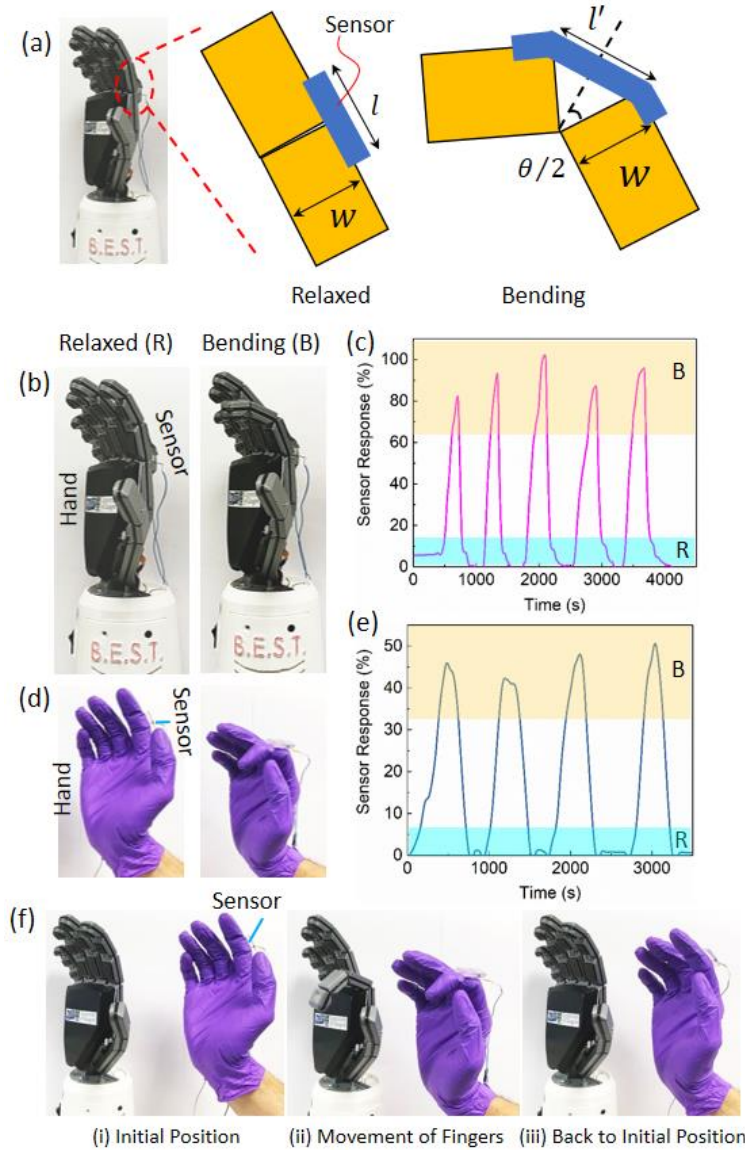
Figure 6: (a) schematic representation of sensor stretching due to the bending of the finger; (b) optical image of the robotic hand with the index finger relaxed (R) and bending (B) condition; (c) temporal response of the sensor due to bending of the finger; (d) optical image of the human hand with the index finger relaxed (R) and bending (B) condition; (e) temporal response of the sensor due to bending of the finger; (f) the optical images of the three steps of the demonstration where the sensor attached in the human finger was taken as feedback to move the robotic finger.

Further, in order to check the feedback control of the sensing system, experiments were also performed with a 3D-printed robotic hand.[35, 36] The robotic hand and wrist were designed using the Computer-Aided-Design (CAD) software SolidWorks 2018 SP4.0 (Dassault Systems, Vélizy-

Villacoublay, France). The hand design was based on the average size of an adult male. The palm

is 85 mm wide, 120 mm long and 30 mm thick. In the palm region, there are cavities for the fingers'

actuators (PQ12-63-6-R micro-linear actuator, Actuonix). More details can be found in a previous

publication of our group[36]. In this case, initially separate experiments were done by attaching the

presented strain sensor on human finger and robotic finger. The calibration of the system was

performed using the stretching experiment. The sensor was fixed in the joints of the phalanges of

robotic and human finger using a double-sided and single-sided adhesive tape. Hence, a bending

of angle θ as shown in **Figure 6(a)** schematically, would lead to stretching of, $\Delta l = l' = 2w \sin(\theta/2)$, where l is the length of the sensor and w is the width of the robotic finger. Hence,

the correlation between the bending angle, θ and stretching, $\Delta l/l$ can be calculated using, $\Delta l/l = l'/l = (2w \sin(\theta/2))/l$. **Figure 6(b)** and **6(d)** shows the optical image of the robotic and human

hand with the sensor attached in index finger in relaxed (R) and bent (B) condition, respectively.

The corresponding response of the sensor from the system is shown in **Figure 6(c)** and **6(e)**,

respectively. The demonstration of the experiment with the robotic hand is shown in Supporting

Video S2. Further, an experiment was performed where the response of the sensor attached in the

human finger was taken as feedback to move the robotic finger. **Figure 6(f)** shows the optical

images of the three steps of this demonstration. The demonstration is shown in the Supporting

Video S3. Details of the circuit is discussed in the Section IV of ESI. **Figure S4** shows the circuit

associated with these experiments. The resolution can be extracted from the experiments

performed with real hand and robotic hand. It was observed from the free bending experiments

that the electrical bending resolution was 150% per degree of free-bending. However, in case of

bending experiments with robotic hand the end of the sensor was attached with the finger and thus

upon bending the sensor underwent axial strain and thus the resolution in that case was quite higher

and similar to starching as discussed later. In that condition, a bending of ~2.7⁰ can be realized using the fabricated sensor as per experiments with a proper circuit arrangement as discussed. The electrical resolution for stretching is quite high ~12k% per percentage of stretching.

The presented sensor was highly sensitive (GF~12000) and shows good performance as demonstrated with human and robotic hand. **Figure 7** shows the graphical representation of the GF with maximum strain value and illustrates where the proposed strain sensor lies compared to prior-art. It is clear from **Figure 7** that the proposed sensor has at least ~400-fold higher sensitivity compared to most of the reported resistive strain sensors. Moreover, it showed significantly high sensitivity among resistive polymer strain sensors reported so far. Further, the proposed sensor shows good linearity up to its maximum starching limit, good resolution in both stretching and bending condition, sufficient dynamic range, and nice stability.
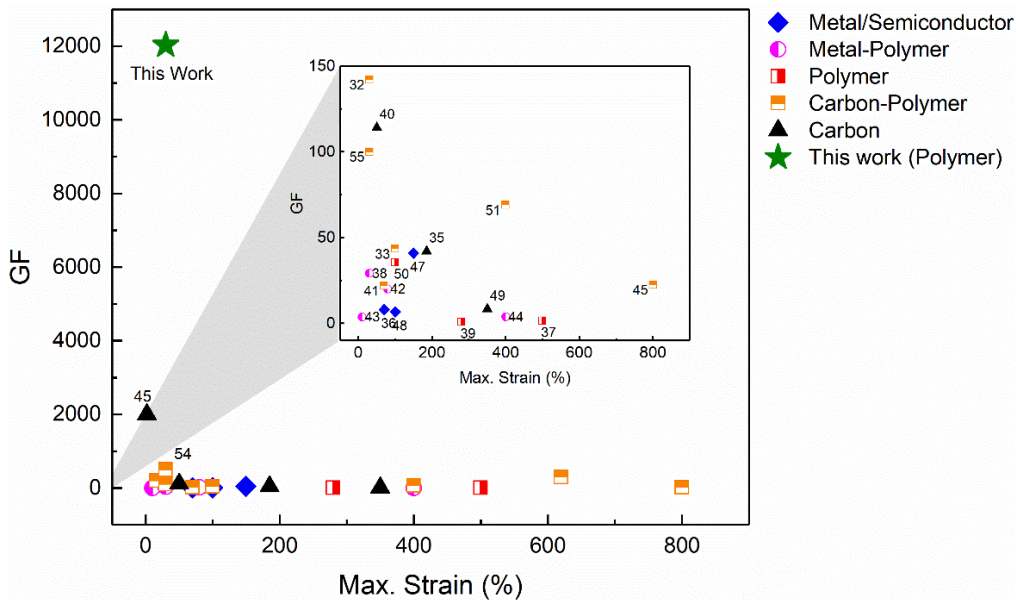

Figure 7: Comparison between previously reported sensors and this work with respect to Gauge factor (GF) vs maximum strain values. The numbers corresponding to each data point in the inset indicate the references from which the data has been obtained.

4. Conclusions

A microchannel based ultrasensitive strain sensor was developed using conductive PEDOT: PSS in PDMS microchannel to measure the strain cycle. The microchannel was fabricated using the replica molding technique with a channel diameter of 175 µm. The response of the sensor was based on the change of electrical resistance due to the variation of effective dimension which creates defects and electrical discontinuities in the polymer upon the applied strain. A theoretical analysis was carried out and compared with the experimental results. We observed about 3 order ($\Delta R/R_0 \sim 1200$) increase in the resistance (R) value for 10% applied strain ($\Delta L/L$, L= length of the sensor) This lead to a gauge factor (GF = $(\Delta R/R_0)/(\Delta L/L)$) of ~ 12000 for 10% applied strain, which is better (~ 400 times) than most of the reported polymer strain sensors. A comparative study was also performed and described in the paper. The average degree of hysteresis (DH) was found to be <9% for the maximum strain condition. Further, experiments were also performed for bending and twisting. It was observed that the sensor is also responsive for different bending and twist angles due to the presence of effective strain in these processes. A response of ($\Delta R/R_0 \sim 250$) and ($\Delta R/R_0 \sim 300$) was recorded for 90º bending and 150º twisting. As a proof of concept, the sensor also was demonstrated with human and robotic hand movement. It was also demonstrated that feedback control can be employed with the strain sensor to control a robotic finger movement using human hand.

AUTHOR INFORMATION

Corresponding Author

*Ravinder Dahiya, Email - Ravinder.Dahiya@gla.ac.uk.

Author Contributions

The manuscript was written through contributions of all authors. All authors have given approval to the final version of the manuscript.

Notes

Any additional relevant notes should be placed here.

ACKNOWLEDGMENT

REFERENCES

[1]   K. Xu, Y. Lu, S. Honda, T. Arie, S. Akita, K. Takei, Journal of Materials Chemistry C 2019, 7, 9609.

[2]   K. Sim, Z. Rao, Z. Zou, F. Ershad, J. Lei, A. Thukral, J. Chen, Q.-A. Huang, J. Xiao, C. Yu, Science Advances 2019, 5, eaav9653.

[3]   R. Dahiya, N. Yogeswaran, F. Liu, L. Manjakkal, E. Burdet, V. Hayward, H. Jörntell, Proceedings of the IEEE 2019, 107, 2016; M. Soni, R. Dahiya, Philosophical Transaction of Royal Society A 2020, 378 20190156.

[4]   F. Yin, H. Lu, H. Pan, H. Ji, S. Pei, H. Liu, J. Huang, J. Gu, M. Li, J. Wei, Scientific reports 2019, 9, 2403.

[5]   R. Dahiya, Proceedings of the IEEE 2019, 107, 247.

[6]   A. Kumar, V. Parab, A. Handu, L. Ding, P. Joshi, C. Jiang, S. Sambandan, Physical Review Applied 2019, 11, 014057; W. Dang, V. Vinciguerra, L. Lorenzelli, R. Dahiya, Flexible and Printed Electronics 2017, 2, 013003.

[7]   W. Dang, L. Manjakkal, W. T. Navaraj, L. Lorenzelli, V. Vinciguerra, R. Dahiya, Biosensors and Bioelectronics 2018, 107, 192.

[8]   C. García Núñez, L. Manjakkal, R. Dahiya, npj Flexible Electronics 2019, 3, 1.

[9]   Y. Jung, K. Jung, B. Park, J. Choi, D. Kim, J. Park, J. Ko, H. Cho, Micro and Nano Systems Letters 2019, 7, 20.

[10]   C. Pang, G.-Y. Lee, T.-i. Kim, S. M. Kim, H. N. Kim, S.-H. Ahn, K.-Y. Suh, Nature materials 2012, 11, 795.

[11]   A. Frutiger, J. T. Muth, D. M. Vogt, Y. Mengüç, A. Campo, A. D. Valentine, C. J. Walsh, J. A. Lewis, Advanced Materials 2015, 27, 2440.

[12]   J. Guo, X. Liu, N. Jiang, A. K. Yetisen, H. Yuk, C. Yang, A. Khademhosseini, X. Zhao, S.-H. Yun, Advanced Materials 2016, 28, 10244.

[13]   R. Sun, B. Zhang, L. Yang, W. Zhang, I. Farrow, F. Scarpa, J. Rossiter, Applied Physics Letters 2018, 112, 251904.

[14]   A. L. Window, *Strain Gauge Technology*, Springer Netherlands, 1992.

[15]   Y. Kanda, Sensors and Actuators A: Physical 1991, 28, 83.

[16]   B. M. Lee, K. J. Loh, Nanotechnology 2017, 28, 155502.

[17]   J. Lee, S. Kim, J. Lee, D. Yang, B. C. Park, S. Ryu, I. Park, Nanoscale 2014, 6, 11932.

[18]   S. Shengbo, L. Lihua, J. Aoqun, D. Qianqian, J. Jianlong, Z. Qiang, Z. Wendong, Nanotechnology 2018, 29, 255202.

[19]   J. Sirohi, I. Chopra, Journal of Intelligent Material Systems and Structures 2000, 11, 246.

[20]   G. Cai, J. Wang, K. Qian, J. Chen, S. Li, P. S. Lee, Advanced science 2017, 4, 1600190; Y. Zheng, Y. Li, Z. Li, Y. Wang, K. Dai, G. Zheng, C. Liu, C. Shen, Composites Science and Technology 2017, 139, 64.

[21]   J. Eom, J.-S. Heo, M. Kim, J. H. Lee, S. K. Park, Y.-H. Kim, RSC Advances 2017, 7, 53373.

[22]   S. Agarwala, G. L. Goh, Y. L. Yap, G. D. Goh, H. Yu, W. Y. Yeong, T. Tran, Sensors and Actuators A: Physical 2017, 263, 593; S. Cheng, Z. Wu, Advanced Functional Materials 2011, 21, 2282; D. M. Vogt, Y. Park, R. J. Wood, IEEE Sensors Journal 2013, 13, 4056; J. Chossat, T.

Yiwei, V. Duchaine, Y. Park, "Wearable soft artificial skin for hand motion detection with embedded microfluidic strain sensing", presented at *2015 IEEE International Conference on Robotics and Automation (ICRA)*, 26-30 May 2015, 2015; J. C. Yeo, J. Yu, Z. M. Koh, Z. Wang, C. T. Lim, Lab on a Chip 2016, 16, 3244; Kenry, J. C. Yeo, J. Yu, M. Shang, K. P. Loh, C. T. Lim, Small 2016, 12, 1593; Y. Jiao, C. W. Young, S. Yang, S. Oren, H. Ceylan, S. Kim, K. Gopalakrishnan, P. C. Taylor, L. Dong, IEEE Sensors Journal 2016, 16, 7870; S. G. Yoon, B. J. Park, S. T. Chang, Sensors and Actuators A: Physical 2017, 254, 1; S. Han, C. Liu, H. Xu, D. Yao, K. Yan, H. Zheng, H.-J. Chen, X. Gui, S. Chu, C. Liu, npj Flexible Electronics 2018, 2, 16; N. Cheng, J. H. Low, B. W. K. Ang, A. J. Y. Goh, C. Yeow, IEEE Sensors Journal 2019, 19, 1269.

[23]   W. Dang, E. S. Hosseini, R. Dahiya, "Soft Robotic Finger with Integrated Stretchable Strain Sensor", presented at *2018 IEEE SENSORS*, 28-31 Oct. 2018, 2018.

[24]   M. Bhattacharjee, M. Soni, R. Dahiya, "Microchannel based Flexible Dynamic Strain Sensor", presented at *2019 IEEE International Conference on Flexible and Printable Sensors and Systems (FLEPS)*, 8-10 July 2019, 2019.

[25]   M. Wang, K. Zhang, X.-X. Dai, Y. Li, J. Guo, H. Liu, G.-H. Li, Y.-J. Tan, J.-B. Zeng, Z. Guo, Nanoscale 2017, 9, 11017; S. Wang, X. Zhang, X. Wu, C. Lu, Soft Matter 2016, 12, 845; S.-J. Park, J. Kim, M. Chu, M. Khine, Advanced Materials Technologies 2016, 1, 1600053; J. D. Pegan, J. Zhang, M. Chu, T. Nguyen, S.-J. Park, A. Paul, J. Kim, M. Bachman, M. Khine, Nanoscale 2016, 8, 17295.

[26]   M. Amjadi, A. Pichitpajongkit, S. Lee, S. Ryu, I. Park, ACS Nano 2014, 8, 5154; N. Lu, C. Lu, S. Yang, J. Rogers, Advanced Functional Materials 2012, 22, 4044; T. Yamada, Y. Hayamizu, Y. Yamamoto, Y. Yomogida, A. Izadi-Najafabadi, D. N. Futaba, K. Hata, Nature Nanotechnology 2011, 6, 296; Y. R. Jeong, H. Park, S. W. Jin, S. Y. Hong, S.-S. Lee, J. S. Ha, Advanced Functional Materials 2015, 25, 4228; J.-H. Kong, N.-S. Jang, S.-H. Kim, J.-M. Kim, Carbon 2014, 77, 199; J. T. Muth, D. M. Vogt, R. L. Truby, Y. Mengüç, D. B. Kolesky, R. J. Wood, J. A. Lewis, Advanced Materials 2014, 26, 6307; C. S. Boland, U. Khan, C. Backes, A. O'Neill, J. McCauley, S. Duane, R. Shanker, Y. Liu, I. Jurewicz, A. B. Dalton, J. N. Coleman, ACS Nano 2014, 8, 8819; B.-U. Hwang, J.-H. Lee, T. Q. Trung, E. Roh, D.-I. Kim, S.-W. Kim, N.-E. Lee, ACS Nano 2015, 9, 8801; S. Gong, D. T. H. Lai, B. Su, K. J. Si, Z. Ma, L. W. Yap, P. Guo, W. Cheng, Advanced Electronic Materials 2015, 1, 1400063; E. Roh, B.-U. Hwang, D. Kim, B.-Y. Kim, N.-E. Lee, ACS Nano 2015, 9, 6252; P. Slobodian, P. Riha, P. Saha, Carbon 2012, 50,

3446; P. R. Slobodian, Pavel; Olejnik, Robert; Matyas, Jiri;, Sensor Review 2018, 38, 163; S. Tadakaluru, W. Thongsuwan, P. Singjai, Sensors 2014, 14; L. Lin, S. Liu, Q. Zhang, X. Li, M. Ji, H. Deng, Q. Fu, ACS Applied Materials & Interfaces 2013, 5, 5815.

[27]   S. Timung, J. Chaudhuri, M. P. Borthakur, T. K. Mandal, G. Biswas, D. Bandyopadhyay, ELECTROPHORESIS 2017, 38, 1450.

[28]   H. Joodaki, M. Panzer, Proceedings of the Institution of Mechanical Engineers, Part H: Journal of Engineering in Medicine 2018, 232, 095441191875980; A. B. Tepole, A. K. Gosain, E. Kuhl, Int J Non Linear Mech 2012, 47, 938.

[29]   L. J. Hart-Smith, Zeitschrift für angewandte Mathematik und Physik ZAMP 1966, 17, 608; D. Ratna, J. Karger-Kocsis, Journal of Materials Science 2008, 43, 254.

[30]   C. R. Siviour, J. L. Jordan, Journal of Dynamic Behavior of Materials 2016, 2, 15; A. Kara, A. Tasdemirci, M. Guden, Materials & Design 2013, 49, 566.

[31]   M. Park, J. Im, M. Shin, Y. Min, J. Park, H. Cho, S. Park, M.-B. Shim, S. Jeon, D.-Y. Chung, J. Bae, J. Park, U. Jeong, K. Kim, Nature Nanotechnology 2012, 7, 803; J. Li, J.-K. Kim, Composites Science and Technology 2007, 67, 2114.

[32]   S. I. White, R. M. Mutiso, P. M. Vora, D. Jahnke, S. Hsu, J. M. Kikkawa, J. Li, J. E. Fischer, K. I. Winey, Advanced Functional Materials 2010, 20, 2709.

[33]   V. B. Shenoy, A. F. Schwartzman, L. B. Freund, International Journal of Fracture 2001, 109, 29; Z. C. Xia, J. W. Hutchinson, Journal of the Mechanics and Physics of Solids 2000, 48, 1107.

[34]   S. G. Yoon, H.-J. Koo, S. T. Chang, ACS Applied Materials & Interfaces 2015, 7, 27562.

[35]   W. Navaraj, R. Dahiya, Advanced Intelligent Systems 2019, 1, 1900051; M. Soni, M. Bhattacharjee, M. Ntagios, R. Dahiya, IEEE Sensors Journal 2020, 1.

[36]   M. Ntagios, H. Nassar, A. Pullanchiyodan, W. T. Navaraj, R. Dahiya, Advanced Intelligent Systems 2019, 1900080 1.